TECHNICAL NOTE

Technical note: Does scan resolution or downsampling impact the analysis of trabecular bone architecture?

Andrea Lukova[1,2] | Christopher J. Dunmore[1] | Zewdi J. Tsegai[3] | Sebastian Bachmann[4] | Alexander Synek[4] | Matthew M. Skinner[2]

[1]Skeletal Biology Research Centre, School of Anthropology and Conservation, University of Kent, Canterbury, UK

[2]Human Origins, Max Planck Institute for Evolutionary Anthropology, Leipzig, Germany

[3]Department of Organismal Biology and Anatomy, University of Chicago, Chicago, Illinois, USA

[4]Computatioal Biomechanics, Institute of Lightweight Design and Structural Biomechanics, Wien, Austria

Correspondence
Andrea Lukova, Max Planck Institute for Evolutionary Anthropology, Leipzig, Germany.
Email: andrea_lukova@eva.mpg.de

Abstract

The "gold standard" for the assessment of trabecular bone structure is high-resolution micro-CT. In this technical note, we test the influence of initial scan resolution and post hoc downsampling on the quantitative and qualitative analysis of trabecular bone in a *Gorilla* tibia. We analyzed trabecular morphology in the right distal tibia of one *Gorilla gorilla* individual to investigate the impact of variation in voxel size on measured trabecular variables. For each version of the micro-CT volume, trabecular bone was segmented using the medical image analysis method. Holistic morphometric analysis was then used to analyze bone volume (BV/TV), anisotropy (DA), trabecular thickness (Tb.Th), spacing (Tb.Sp), and number (Tb.N). Increasing voxel size during initial scanning was found to have a strong impact on DA and Tb.Th measures, while BV/TV, Tb.Sp, and Tb.N were found to be less sensitive to variations in initial scan resolution. All tested parameters were not substantially influenced by downsampling up to 90 μm resolution. Color maps of BV/TV and DA also retained their distribution up to 90 μm. This study is the first to examine the effect of variation in micro-CT voxel size on the analysis of trabecular bone structure using whole epiphysis approaches. Our results indicate that microstructural variables may be measured for most trabecular parameters up to a voxel size of 90 μm for both scan and downsampled resolutions. Moreover, if only BV/TV, Tb.Sp or Tb.N is measured, even larger voxel sizes might be used without substantially affecting the results.

KEYWORDS
anisotropy, bone volume, resolution, trabecular bone, trabecular number, trabecular spacing, trabecular thickness, voxel size

1 | INTRODUCTION

Trabecular bone is a porous tissue found in the epiphyses of long, short, and irregular bones (Keaveny et al., 2001). Although the structure of trabecular bone is partially genetically determined (Loewen et al., 2016; Paternoster et al., 2013; Turner et al., 2000), (re)modeling

is at its peak during growth and gradually declines into adulthood (Glatt et al., 2007; Halloran et al., 2002; Saers et al., 2020; Seeman, 2003; Su et al., 2013). Trabecular bone tissue is thought to respond to biomechanical forces and functionally adapt to its mechanical environment (Ruff et al., 2006). In places where incurred load is lower, there is thought to be a reduction in the amount of trabecular

bone, resulting in a weaker structure (Schulte et al., 2013). Conversely, in places where stress is higher, there should be an increase in trabecular tissue, resulting in a stronger bone structure (Barak et al., 2011; Pontzer et al., 2006; Schulte et al., 2013; Sinclair et al., 2013). These changes in trabecular bone architecture can include the thickness of trabecular struts, their spacing, and their orientation. Therefore, analysis of trabecular structure can provide insights into the biomechanical loads incurred by bones during life. It can be used to understand the skeletal morphology of living taxa and reconstruct behavior in fossil taxa (Kivell, 2016; Komza, & Skinner, 2019; Ryan & Shaw, 2012; Saers et al., 2020).

The traditional method of analyzing trabecular structure in 3D is to quantify trabecular bone in a volume of interest (VOI). The main advantage of the VOI method is that it allows for the extraction and quantification of a portion of a complex structure from a much larger micro-CT data set. However, defining a homologous VOI, both its size and location, is far from straightforward, especially across taxa and/or an ontogenetic series where there can be substantial differences in both size and morphology (Gross et al., 2014; Kivell et al., 2011; Lazenby et al., 2011). Moreover, the region of trabecular structure that differs most amongst the study sample could be outside of the VOI region when determined a priori. More recently, several studies have placed multiple VOIs throughout an anatomical region, revealing the presence of regional differences in trabecular bone structsure (DeSilva & Devlin, 2012; Griffin, 2018; Su et al., 2013). Some studies used geometric morphometrics (GM), where sliding semilandmarks are used to define homologous locations across surfaces in order to place multiple VOIs, to assess trabecular variation beneath the articular surfaces of the talus and distal femur (Sylvester & Terhune, 2017), in the metacarpals (e.g., Dunmore et al., 2019; Dunmore, Bardo, Skinner, & Kivell, Dunmore, Bardo, et al., 2020) and in the proximal femur (Georgiou et al., 2020). Furthermore, a method originally developed for finite-element material-mapping (Pahr & Zysset, 2009), has been adapted for analyses of high-resolution trabecular bone across primates (Gross et al., 2014; Tsegai et al., 2013). Holistic morphometric analysis (HMA) quantifies trabecular morphology through the entire epiphysis rather than in one or a few sub-surface VOIs. Recently, Bachmann et al. (2022), developed HMA with a canonical holistic approach (cHMA), which allows for statistical comparisons of trabecular patterns between groups, free of a priori subsampling, by calculating mean models that contain homologous spatial units of analysis.

Studies of trabecular bone architecture often analyze scans with different resolutions across the studied species and/or individuals (Cazenave et al., 2019; Georgiou et al., 2018; Lukova et al., 2024; Sylvester & Terhune, 2017). This can be due to collection of micro-CT scans by different researchers with different protocols, due to specimen size limiting resolution on different CT systems, or scans may be downsampled (i.e., process of reducing the resolution or dimensions of a digital image by decreasing the number of pixels in the image) after collection due to the computational limitations of processing large datasets. Previous studies have shown that downsampling can impact the accuracy and precision of measurements of trabecular architecture. For example, trabecular thickness (Tb.Th) (Isaksson
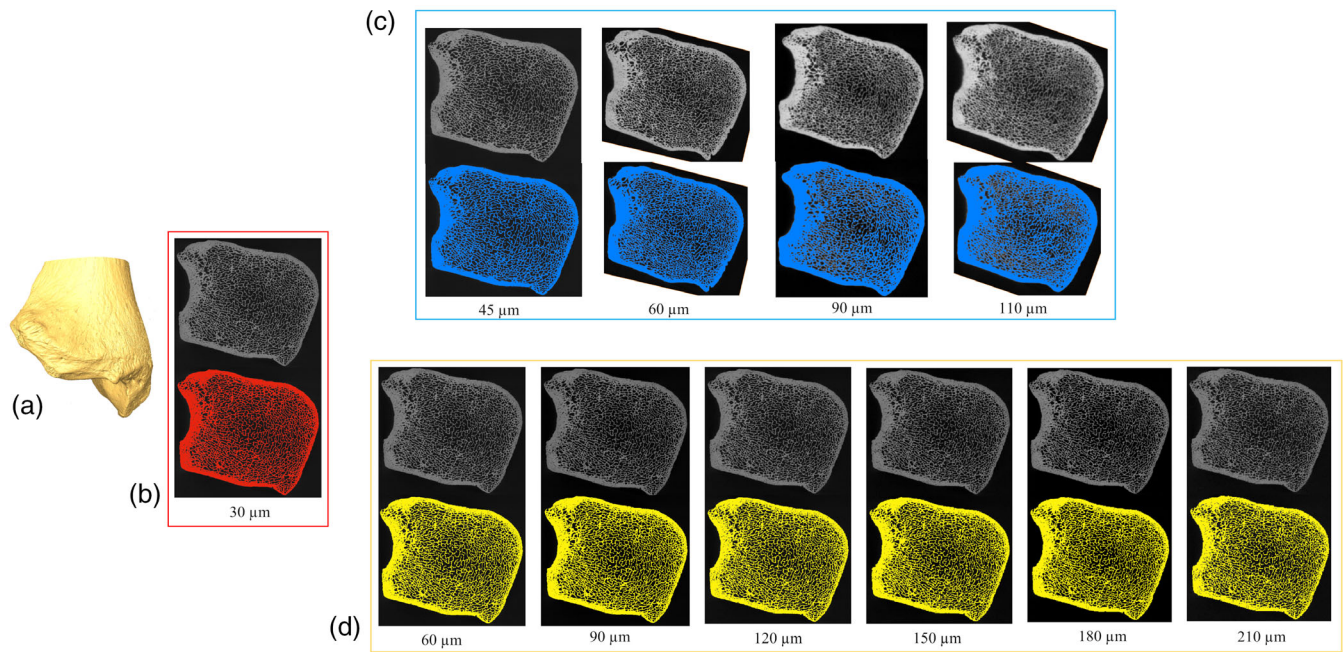
et al., 2011; Kothari et al., 1998; Majumdar et al., 1996; Muller et al., 1996; Sode et al., 2008) or measures of anisotropy can be highly sensitive to voxel size (Isaksson et al., 2011; Kothari et al., 1998; Sode et al., 2008). In general, it is expected that lower resolutions (the lower resolution the larger voxel size) create blur in the scan images making some features hard to segment and may lead to loss of thin trabeculae, that is, if the feature is smaller than the voxel size it may well be averaged out in favor of another phase such as background (partial volume averaging). Majumdar et al. (1996) showed that Tb.Th tends to be increasingly overestimated at lower resolutions when analyzing magnetic resonance (MR) and micro-CT images. Similarly, Müller et al. (1996) found that trabecular spacing and number can be precisely measured at resolutions up to 175 μm, however, Tb.Th required a much higher resolution for accurate assessment. Moreover, Isaksson et al. (2011), using micro-CT scans, found that with decreasing resolution, the originally detected differences between normal and osteoporotic groups diminished. Kim et al. (2004) used three different scanning and voxel sizes a high-resolution voxel size (21 μm), a commonly used intermediate voxel size (50 μm), and a voxel size applicable to scans of whole human vertebral bodies (110 μm) to examine the effect of voxel size on stereological measures of human trabecular bone. They found that the error in stereological parameters ranged from 0.1% to 102% depending on the voxel size analyzed. Peyrin et al. (1998) examined a series of vertebral samples with voxel sizes of 1.4, 6.7, and 14 μm. They concluded that voxel sizes as large as 14 μm provide a reasonably accurate measurement of trabecular architecture. Christiansen (2016) investigated micro-CT scans of mouse trabecular bone measures with voxel sixes at 6–30 μm. They demonstrated that voxel size strongly affects connectivity density and Tb.Th. All these studies suggest that high resolution scans should be used, when possible, to accurately measure trabecular bone microstructure.

In this study, we test the impact of (1) scanning the same specimen at different resolutions and (2) downsampling a high-resolution scan of this specimen to lower resolutions using a whole-epiphysis approach. The trabecular variables tested include bone volume fraction (BV/TV), degree of anisotropy (DA), Tb.Th, trabecular spacing (Tb.Sp), and trabecular number (Tb.N). We also assess the impact of scan resolution and downsampling on material maps of BV/TV and DA, which are some of the most biomechanically informative aspects of trabecular architecture and are widely reported in the literature (Goldstein et al., 1993; Odgaard et al., 1997; Van Rietbergen et al., 1998).

2 | MATERIALS AND METHODS

The study sample of micro-CT scans of varying resolutions was created from scans of a complete right distal tibia of a *Gorilla gorilla* individual from Cameroon, curated at the Powell-Cotton Museum in Birchington-on-Sea, UK.

The specimen was scanned using a Diondo D1 scanner at the Imaging Centre for Life Sciences at the University of Kent (Canterbury, UK). The scan parameters included an acceleration voltage of 130 kV, a tube current of 130 μA and a 1.0 mm aluminium filter. Images were reconstructed as 16-bit TIFF stacks.

LUKOVA ET AL.

AMERICAN JOURNAL OF
BIOLOGICAL ANTHROPOLOGY
The Official Journal of the American Association of Biological Anthropologists

WILEY 3 of 14

FIGURE 1 (a) Surface of the studied distal tibia region (anterior view); (b) unsegmented (raw) and overlapping segmented high-resolution scan (in distal view) with voxel size of 30 μm used as the baseline scan; (c) serial unsegmented and overlapping segmented images of the same distal tibia (in distal view) scanned under the lower resolution with four different voxel sizes of 45, 60, 90, and 110 μm; (d) the baseline scan downsampled to voxel size of 60, 90, 120, 150, 180, and 210 μm.

**TABLE 1** Segmentation parameters.

Method	Resolution (μm)	Trabecular thickness (mm)[*]	Trabecular thickness/resolution (mm/μm)	Grid size (px)	Number of classes	Probability filter
Baseline scan	30	0.27	9.0	10	2	None
Downsampled	60	0.28	4.7	5	2	None
Downsampled	90	0.31	3.4	5	2	None
Downsampled	120	0.33	2.8	5	2	None
Downsampled	150	0.35	1.9	5	2	None
Downsampled	180	0.37	2.0	5	2	None
Downsampled	210	0.37	1.8	5	2	None
Rescanned	45	0.40	8.9	10	2	None
Rescanned	60	0.32	5.3	10	2	None
Rescanned	90	0.39	4.3	5	2	None
Rescanned	110	0.45	4.1	5	2	None

*Measured in a 2D cross-section.

Two samples were created to test the impact of voxel resolution on the measurement and visualization of trabecular architecture. In the first, the tibia was rescanned four additional times to produce volumes with voxel sizes of 45, 60, 90, and 110 μm (Figure 1c). To create the second sample, a scan with a voxel size of 30 μm was downsampled to 60, 90, 120, 150, 180, and 210 μm (Figure 1d). Downsampling was conducted in medtool v4.5 (www.dr-pahr.at/medtool) using whole-integer factors only to avoid aliasing (for more details on aliasing, see for example, He et al., 2021; Tward & Siewerdsen, 2009; Yen et al., 1999; Zbijewski & Beekman, 2003). For example, when

downsampling 30 to 60 μm eight (2^3) voxels are averaged and from 30 to 90 μm 27 (3^3) voxels are averaged.

All images were segmented into a binary phase of background and bone using the MIA-clustering algorithm (Dunmore et al., 2018). This method requires the definition of a grid size, which was selected by measuring the thickness of the thickest trabeculae in a 2D cross-section using Avizo to determine their width in pixels. The grid size was then set a few voxels larger then this measurement to ensure that the local segmentation focused on features within the phase of interest (Table 1) (Dunmore et al., 2018). Two classes were used for all
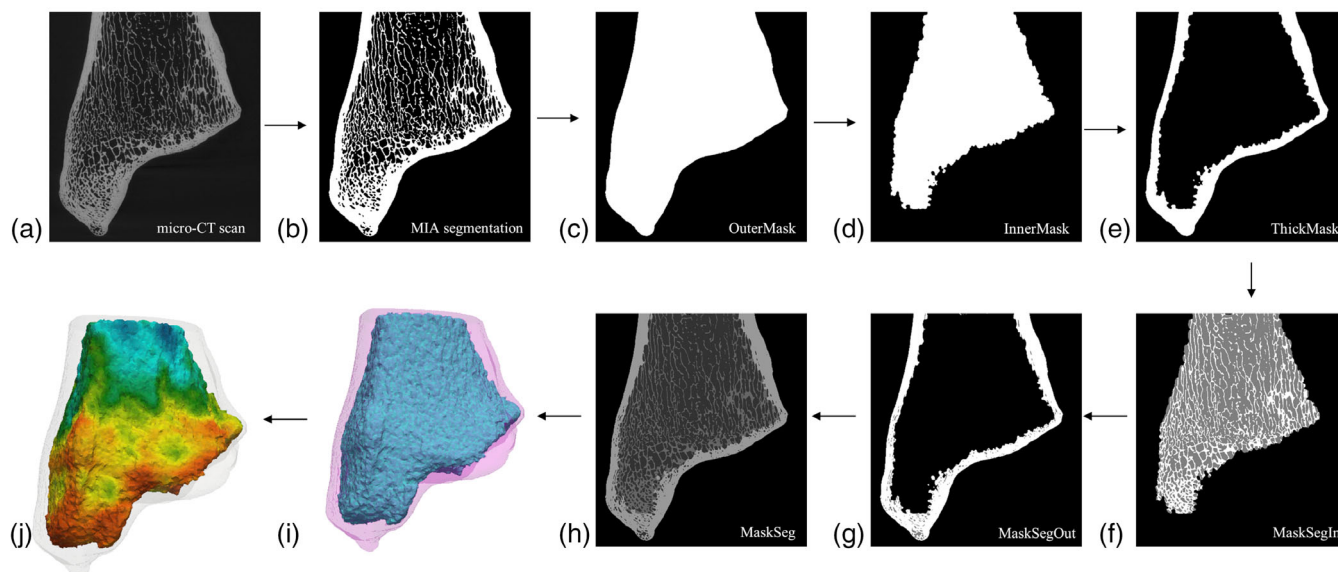
FIGURE 2   Workflow of medtool processing steps (posterior view). (a) Original micro-CT scan; (b) results of the MIA binary segmentation process; (c) *OuterMask*; (d) *InnerMask*; (e) *ThickMask*; (f) *MaskSegIn*; (g) *MaskSegOut*; (h) *MaskSeg*; (i) finite element model of the cortical (pink) and trabecular (blue) area; (j) BV/TV representation. BV/TV, bone volume.

scans (Table 1). To assess if the same volume of bone was segmented in each image stack, we measured segmented BV/TV for each scan in Avizo 6.3 (Visualization Science Group, SAS). Each segmented image was then used for further analysis of trabecular parameters (Figure 2).

The external and inner volumes of all images were defined using medtool v4.5 (www.dr-pahr.at/medtool) and taken from each other to produce the thick cortical bone shell, following published protocols (Gross et al., 2014; Pahr & Zysset, 2009; Tsegai et al., 2013). The binary images (in which bone voxels can be classified as 1 and non-bone voxels as 0) from MIA (Figure 2b) were used as inputs for medtool. The primary structure in the image was identified with a grayscale value of one (white voxels). Subsequently, any floating voxels that were not contiguous with the bone were set to zero or black. Morphological filters in medtool were then applied to fill the bone, thereby isolating the external and internal edges of the cortical bone in 3D. This process resulted in a mask delineating the internal BV/TV and outer cortical bone. During the bone filling process, small pores within the cortical bone were identified and filled based on the size of the kernel radius. This method ensured that the fine porosity of the cortical bone was preserved, while moderate gaps indicative of genuine variations in trabecular shape or separation were maintained. For this, a ray-casting method was used. Subsequently, closing, and opening operations were performed to fill in the gaps in the bone structure, resulting in the creation of the *OuterMask* (Figure 2c). To identify trabecular spaces, the same ray casting process was employed, but with a starting point at the edge of the *OuterMask* instead of the image edge. Rays terminated upon encountering air voxels rather than bone voxels. Closing and opening operations were then applied to fill in areas where rays had traversed directly through trabeculae, thus closing voids in the *InnerMask* (Figure 2d). The *OuterMask* delineated the overall geometry of the entire bone by detecting its outer contour

using rays. Conversely, the *InnerMask* served a similar purpose to the *OuterMask*, but specifically defined the 3D geometric boundaries of the trabecular bone region within the entire bone structure. Once both masks were completed, medtool subtracted the *InnerMask* from the *OuterMask* and created a "*ThickMask*" (Figure 2e), which specifically represented the thickness of the cortical bone. Following the creation of *InnerMask*, *OuterMask*, and *ThickMask*, medtool generated three final volumes for subsequent analysis. *MaskSegIn* (Figure 2f) represented the trabecular bone and internal spaces. It was derived from *OuterMask* with *ThickMask* removed, focusing solely on the trabecular bone and internal spaces. *MaskSegOut* (Figure 2g) represented the cortical bone, including its pores. It was derived from *InnerMask* with *OuterMask* removed, isolating only the cortical bone. *MaskSeg* (Figure 2h) represented all elements including cortical bone, pores, trabeculae, and internal spaces. *MaskSeg* was created by combining *MaskSegIn* and *MaskSegOut*.

The CGAL (Computational Geometry Algorithms Library, https://www.cgal.org) 4.9 mesher was then applied to the *InnerMask* and *OuterMask* to create a tetrahedral mesh of both the trabecular volumes (Figure 2i). This mesh was created for each resolution separately and all meshes were later used for data visualization. Each mesh underwent optimization through a series of iterative processes to achieve a smooth boundary, ensuring there were no overlaps or holes between the tetrahedra. Tetrahedra were chosen over hexahedra because their geometry results in a smoother boundary, minimizing the loss of trabecular architectural information (Alberich-Bayarri et al., 2008; Müller, & Rüegsegger, 1996; Ulrich et al., 1999). To gather material property data, a 3D grid with 2.5 mm cells was placed as a bounding box over the *MaskSegIn*. Subsequently, a 5 mm sampling sphere moved between the grid nodes across the entire bounding box, iteratively measuring trabecular parameters. By aligning the finite element

LUKOVA ET AL.

AMERICAN JOURNAL OF
BIOLOGICAL ANTHROPOLOGY
The Official Journal of the American Association of Biological Anthropologists

WILEY | 5 of 14

mesh with the nodes of the sampling sphere, each of the trabecular parameters was interpolated onto the mesh. When all these steps were taken, HMA was completed, and trabecular parameters were measured within the bone. Trabecular parameters were measured by the mia-multi module in medtool. Medtool outputted quantitative data as well as options for the quantitative visualization of the data. These interpolated meshes are visualized in Paraview 4.8.2 (Ahrens et al., 2006) (Figure 2j).

The measure of BV/TV is the proportion of trabecular bone of the total volume in each region and was calculated as the ratio of bone voxels to non-bone voxels within the masked volume of each sampling sphere (VOI). DA in 3D was calculated using the mean-intercept-length method (Odgaard et al., 1997; Whitehouse, 1974). The value of DA is zero if the minor and major eigenvectors are of equal magnitude (i.e., isotropic), and is one if the minor and major eigenvectors are maximally different (i.e., anisotropic). A value between 0 and 1 is produced via the formula 1–(min. eigenvalue/max. eigenvalue) (Kivell et al., 2011). To calculate Tb.Th, medtool computed the distance map of the bone voxels of the *MaskSegIn* (Figure 2f) and extracted the distance ridge from which the average distance was calculated. Tb.Sp was calculated in a similar way by inverting bone and background labels. Tb.N was calculated using Tb.Th and Tb.Sp via the formula 1/(Tb.Th + Tb.Sp).

Boxplots and histograms summarizing the data distribution of each variable were generated directly from all VOIs of each respective scan. Shapiro–Wilk tests were used to assess normality and Levene's tests were used to assess equality of variance of each trabecular variable (Tables S1–S5 and Figure S4). Kruskal–Wallis and Dunn's post hoc tests were used to test if the means of a specific parameter differed significantly between datasets. The differences were tested between all combinations of groups within the downsampled images and then separately within the rescanned images. All statistical analyses were conducted in R v3.4.1 and plots were generated using the ggplot2 package (R Core Team, 2017; Wickham, 2016).

3 | RESULTS

3.1 | Total bone volume

The total segmented BV/TV for the 30 μm scan is 28,082 mm^3 (Table 2). When downsampling, the segmented BV/TV remains similar until 210 μm, at which point there is a reduction of 0.7% (27,897 mm^3) (Table 2). Rescanning the specimen results in a stepped increase at 45 (1.5%) and 60 (2.1%) μm, with the segmented volume then remaining similar in scans at 90 and 110 μm (Table 2).

3.2 | Bone volume fraction

Distributions of BV/TV values for each VOI of the background grid in the baseline scan, downsampled volumes and rescanned volumes are presented in Figure 3. The variance of BV/TV values remains

TABLE 2 Segmented bone volume for all tested CT scans.

Voxel size (μm)	Technique	Segmented bone volume (mm3)	Segmented bone volume change (%)
30	Baseline micro-CT scan	28,082	0.00
60	Downsampled	28,037	−0.16
90		28,058	−0.09
120		27,985	−0.35
150		28,061	−0.08
180		28,118	0.13
210		27,897	−0.66
45	Rescanned	28,505	1.51
60		28,674	2.11
90		28,682	2.14
110		28,700	2.20

relatively similar for all scans and any outliers represent the elements with both lowest and highest BV/TV values. When downsampling, there appears to be a slight decrease in median BV/TV values compared to the baseline scan (Figure 3a), however, the distributions strongly overlap. When rescanned at 45 μm, the median BV/TV is similar, but then increases slightly at voxel sizes of 60, 90, and 110 μm. Similarly, histograms of BV/TV values from each VOI show that the general data distribution pattern remains stable and not normally distributed across all voxel sizes using both downsampled and rescanned images (Figure 3b,c; Table S1). Table 3 shows that the mean BV/TV values (of the VOI's) gradually decrease with downsampling (reaching 12.1% at 210 μm). Rescanning at 45 μm results in a mean BV/TV decrease (0.64%), while there are increases in mean BV/TV at 60 (8.06%), 90 (3.87%), and 110 μm (5.81%) compared to the baseline scan (Table 3).

The Kruskal–Wallis test shows a statistically significant difference in BV/TV within the downsampled and (separately) within the scanned images (Table 4). Additionally, a Dunn's post hoc test was performed to further explore these differences. The post hoc tests indicate that there are significant differences in BV/TV within all combinations of downsampled and scanned images (Table S6).

To understand if any of these outliers are spatially organized, and thus potentially affecting functional interpretations, we visualized the BV/TV distribution throughout the distal tibia for the baseline scan and all downsampled and rescanned volumes. Figure 4 shows the colourmaps, that is, interpolations of the values from the VOI's discussed above, of BV/TV distribution. Compared to the baseline scan (Figure 4a), the general pattern of BV/TV distribution is maintained in all downsampled images, up to a voxel size of 210 μm (Figure 4b). In this volume the region of highest BV/TV (in red) extends further above the malleolus and is more concentrated in the malleolar groove and, in the mid-coronal view, the region of highest BV/TV is concentrated more laterally and BV/TV is lower in the malleolar region
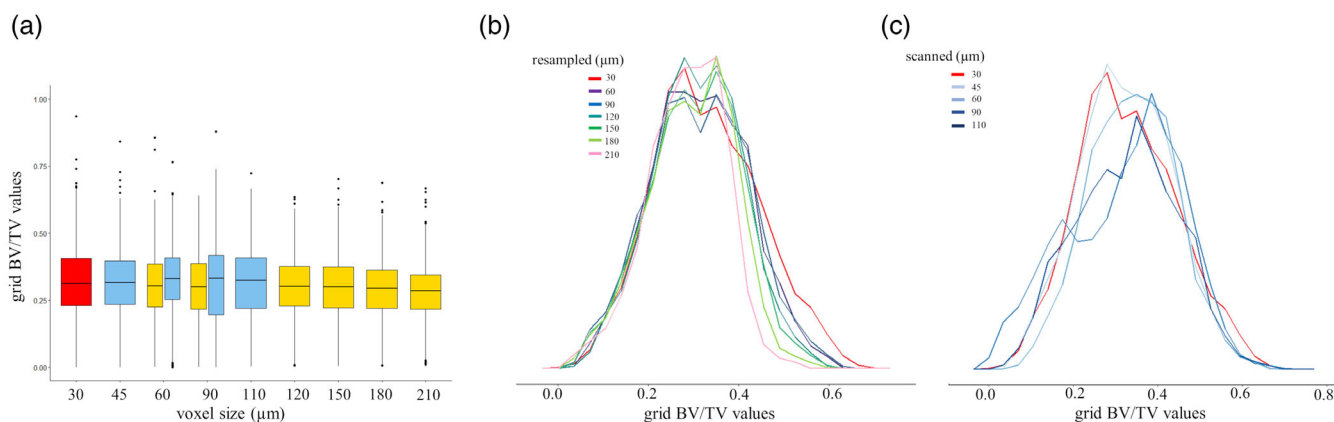
FIGURE 3 (a) Boxplots of the grid BV/TV values for each voxel size for the baseline scan (red), the downsampled data (yellow) and for the specimen scanned at different resolution (blue); (b) histogram of the grid BV/TV values for each voxel size for the baseline scan (red line) and the downsampled data; (c) histogram of the grid BV/TV values for each voxel size for the baseline scan (red line) and for the specimen scanned at different resolution. BV/TV, bone volume.

TABLE 3 The mean and SD values of all tested trabecular parameters.

Voxel size (μm)	Technique	Mean BV/TV (SD)	Mean DA (SD)	Mean Tb. Th (SD)	Mean Tb. Sp (SD)	Mean Tb. N (SD)	N of grid nodes*
30	Baseline micro-CT scan	0.313 (0.105)	0.470 (0.112)	0.272 (0.081)	0.759 (0.267)	1.001 (0.154)	734,423
60	Downsampled	0.301 (0.098)	0.498 (0.117)	0.291 (0.078)	0.786 (0.786)	0.954 (0.136)	648,989
90		0.302 (0.099)	0.479 (0.116)	0.316 (0.080)	0.802 (0.252)	0.916 (0.124)	646,690
120		0.299 (0.095)	0.421 (0.105)	0.338 (0.076)	0.818 (0.247)	0.885 (0.118)	683,156
150		0.293 (0.091)	0.353 (0.092)	0.370 (0.072)	0.846 (0.244)	0.840 (0.108)	535,414
180		0.284 (0.087)	0.296 (0.079)	0.404 (0.061)	0.873 (0.242)	0.799 (0.101)	527,357
210		0.275 (0.086)	0.261 (0.074)	0.446 (0.048)	0.905 (0.240)	0.754 (0.093)	573,089
45	Rescanned	0.311 (0.101)	0.488 (0.114)	0.295 (0.085)	0.783 (0.264)	0.954 (0.140)	699,828
60		0.335 (0.094)	0.481 (0.114)	0.336 (0.092)	0.777 (0.254)	0.918 (0.119)	668,455
90		0.322 (0.128)	0.420 (0.102)	0.427 (0.112)	0.921 (0.278)	0.768 (0.121)	682,908
110		0.328 (0.107)	0.391 (0.102)	0.442 (0.116)	0.859 (0.249)	0.781 (0.087)	583,379

*Number of intrenal grid nodes on which each VOI is centred.

(Figure 4b). The BV/TV concentration on the posterior side of the malleolus, as well as anteriorly and posteriorly on the articular surface, is also higher at the downsampled voxel size of 210 μm (see the distal view Figure 4b). Rescanning at 60 μm presents a broadly similar pattern of BV/TV on each surface and in the mid-coronal cross section (Figure 4c). However, after rescanning at 90 and 110 μm the distribution pattern is less consistent. The high BV/TV concentration along the malleolar region and under the articular surface is lost (see mid-coronal view in Figure 4c).

3.3 | Degree of anisotropy

Downsampling from the baseline to 60 and 90 μm does not result in a large change in DA values; however, there is a marked reduction in DA when downsampling between 120 and 210 μm (Figure 5). Similarly, rescanning at 45 and 60 μm does not result in a change in DA,

but DA drops to a greater degree in scans at 90 and 110 μm. The general DA data distribution for the baseline scan is not normally distributed and overlaps across all scan voxel sizes (Figure 5b; Table S3), even in the downsampled voxel size of 90 μm (Figure 5b). However, the data moves towards an apparent positively skewed distribution pattern when downsampled to 120–210 μm (Figure 5b; Table S2). Table 3 shows that mean DA values are closest to the baseline scan at downsampled voxel sizes of 60 and 90 μm and the lowest mean DA values drop 44.5% from the baseline scan at 210 μm. The mean DA values are close to the baseline in rescans at 45 and 60 μm, while there is a 19.9% drop in DA when rescanned at 110 μm (Table 3).

The Kruskal–Wallis test shows a statistically significant difference in DA within the downsampled and scanned images (Table 4). Additionally, the Dunn's post hoc test indicates that there are significant differences in DA within all combinations of downsampled and scanned images (Table S6).

LUKOVA ET AL.

AMERICAN JOURNAL OF
BIOLOGICAL ANTHROPOLOGY
The Official Journal of the American Association of Biological Anthropologists

WILEY | 7 of 14

TABLE 4 The Kruskal-Wallis test for BV/TV, DA, Tb.Th, and Tb. Sp grid values within downsampled and scanned images.

Technique	Df	Chi-squared	p-value
BV/TV			
Downsampling	6	11,400	**<0.001**
Scanning	4	6025	**<0.001**
DA			
Downsampling	6	399,906	**<0.001**
Scanning	4	95,682	**<0.001**
Tb.Th			
Downsampling	6	16,247	**<0.001**
Scanning	4	7770	**<0.001**
Tb.Sp			
Downsampling	6	1907	**<0.001**
Scanning	4	864	**<0.001**
Tb.N			
Downsampling	6	6100	**<0.001**
Scanning	4	3352	**<0.001**

Note: Significance bold value represents $\alpha = 0.05$.

Figure 6 shows colourmaps of the DA distribution throughout the distal tibia for the baseline scan and all downsampled and rescanned volumes. The DA colourmaps are more impacted by voxel sizes compared to the BV/TV distribution maps. Compared to the baseline scan (Figure 6a), the general pattern of DA distribution is consistent in all downsampled images until the voxel size of 120 μm (Figure 6b). The general DA distribution pattern is visible even at the downsampled voxel size of 150 μm. However, in this volume the low DA (blue color) starts to be concentrated randomly above the articular surface where high DA is found in higher resolution scans (see mid-coronal view in Figure 6c). This is even more apparent in the larger voxel sizes of 180 and 210 μm. The general DA distribution pattern of the baseline scan disappears completely at a voxel size of 210 μm and high DA is inconsistently concentrated throughout the distal tibia (Figure 6b). Rescanning at 60 μm presents a broadly similar pattern of DA on each surface and in the cross-section (Figure 6c). However, after rescanning at 90 and 110 μm the distribution pattern becomes less consistent. The high DA values are lost laterally above the articular surface at a rescanning voxel size of 90 μm and medially above the malleolus at a voxel size of 110 μm (see mid-coronal view in Figure 6c).

3.4 | Trabecular thickness, spacing, and number

Distributions of Tb.Th, Tb.Sp, and Tb.N values for each VOI of the background grid for the baseline scan, downsampled, and rescanned volumes are presented in Figure 7. Voxel size changes in both rescanning and downsampling images has the strongest effect on the quantification of Tb.Th and a weaker effect on the quantification of Tb.Sp and Tb.N (Figure 7). The outliers represent the elements with the lowest/highest Tb.Th (Figure 7a), Tb.Sp (Figure 7b), and Tb.N (Figure 7c).

In both downsampled and rescanned images, median values of Tb.Th and Tb.Sp increase gradually, while median values of Tb.N decrease gradually across all voxel sizes compared to baseline scan (Figure 7). When scanning at different resolutions, the Tb.Sp range remains approximately the same up to a voxel size of 60 μm compared to the baseline scan (Figure 7b), however, the distributions overlap across all voxel sizes.

Table 3 shows that mean Tb.Th values gradually increase with increasing voxel size in both downsampled (reaching 64.0% at 210 μm) and rescanned (reaching 62.5% at 110 μm) images. The mean Tb.Sp values are unstable with increasing voxel size in both downsampled (reaching highest increase 194.4% at 60 μm and highest decrease 11.1% at 210 μm) and rescanned (reaching highest increase 4.1% at 90 μm and highest decrease 6.7% at 110 μm) images compared to the baseline scan (Table 3). The mean Tb.N values gradually decrease with increasing voxel size in downsampled (reaching 24.7% at 210 μm) images compared to the baseline scan (Table 3). Mean Tb.N drops off 23.3% at a rescanned voxel size of 90 μm compared to the baseline scan and increases again at 110 μm (reaching 1.7%) compared to the 90 μm scan (Table 3).

The Kruskal–Wallis test shows a statistically significant difference in Tb.Th, Tb.Sp, and Tb.N within the downsampled and scanned images (Table 4). Additionally, the Dunn's post hoc test indicates that there are significant differences in Tb.Th, Tb.Sp, and Tb.N within most combinations of downsampled and scanned images (Table S7). There are no significant differences in Tb.Sp between the downsampled 60 and 90 μm datasets or between scanned voxel sizes of 45 and 90 μm. Moreover, there is no significant difference in Tb.N between scanned voxel sizes of 60 and 110 μm (Table S7).

Colourmaps of the Tb.Th, Tb.Sp, and Tb.N distribution are presented as supporting information (Figures S1–S3). Compared to the baseline scan, the general pattern of the Tb.Th distribution is consistent when downsampled to 150 μm and rescanned at 45 μm (Figure S1). Tb.Th values are higher in the malleolus and under the articular surface and lower above the articular surface when downsampled to 210 μm (see the cross-section mid-coronal view in the Figure S1b). Tb.Th values are lower across the entire distal tibia at rescanned voxel sizes of 90 and 110 μm (Figure S1c). The general pattern of the Tb.Sp distribution is consistent for all images up to a voxel size of 60 μm (Figure S2). The Tb.Sp values are lower in the malleolus and under the articular surface when rescanned at 90 μm compared to the baseline scan (Figure S2c). The Tb.Sp values in the malleolus are higher at 110 μm compared to the baseline scan (see the mid-coronal view in Figure S2c). The general pattern of Tb.N distribution is consistent when downsampled to 150 μm and rescanned at 110 μm (Figure S3). However, in both cases, high Tb.N values above the articular surface are spread more broadly across all voxel sizes compared to the baseline scan (see the mid-coronal view in the Figure S3).

4 | DISCUSSION

This study investigated the impact of voxel size (in downsampled and rescanned micro-CT volumes) on the quantification of trabecular bone
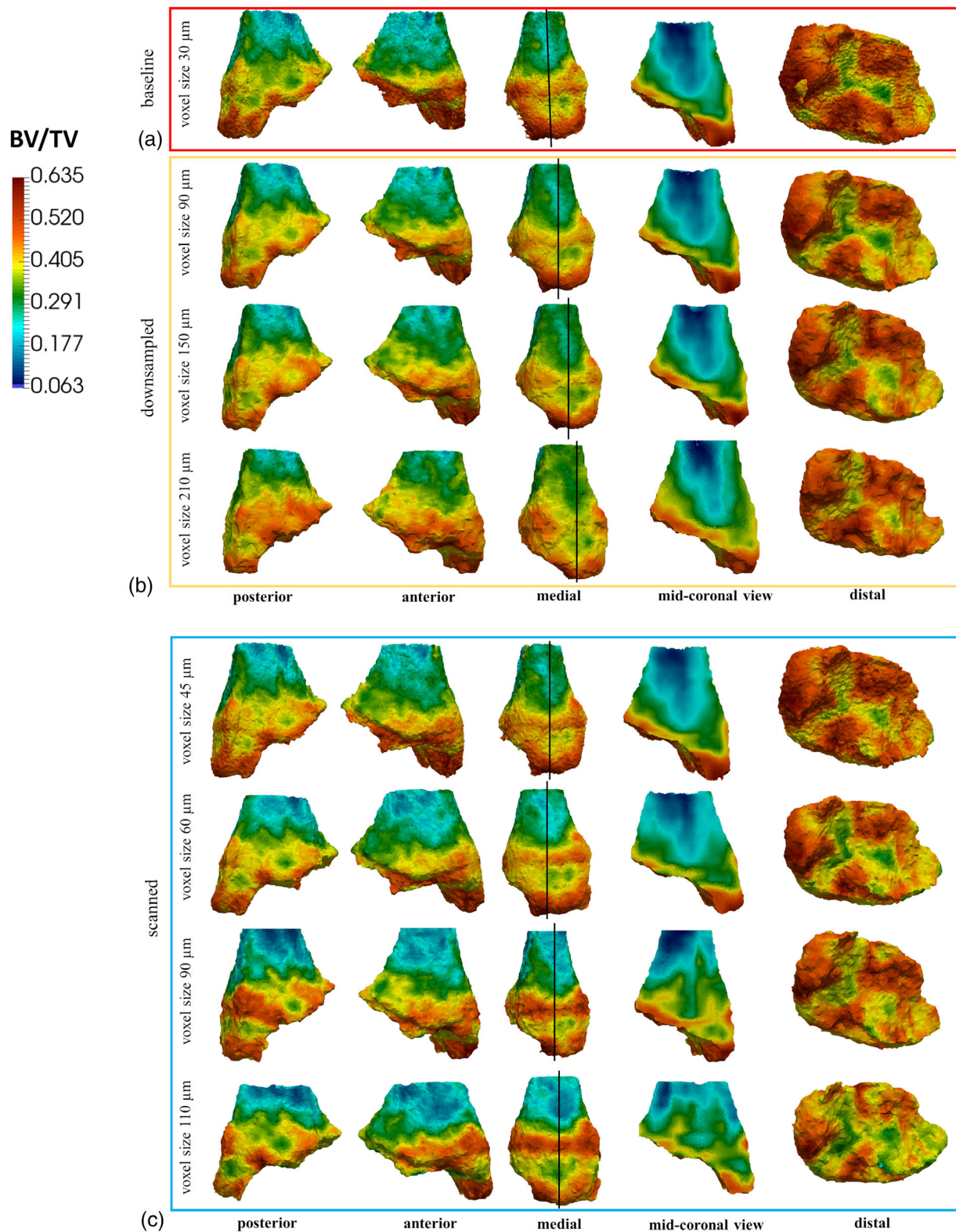
FIGURE 4   Distal tibia model of BV/TV distribution of tested *Gorilla* individual for baseline scan (a), downsampled voxel sizes of 90, 150, and 210 μm (b), and scan voxel sizes of 45–110 μm (c). Vertical lines through the medial view show where the slices are positions for the cross-section mid-coronal view. Dark red represents the highest and dark blue the lowest BV/TV values. All colourmaps were scaled to baseline scan data range. BV/TV, bone volume.

LUKOVA ET AL.

AMERICAN JOURNAL OF
BIOLOGICAL ANTHROPOLOGY
The Official Journal of the American Association of Biological Anthropologists

WILEY 9 of 14
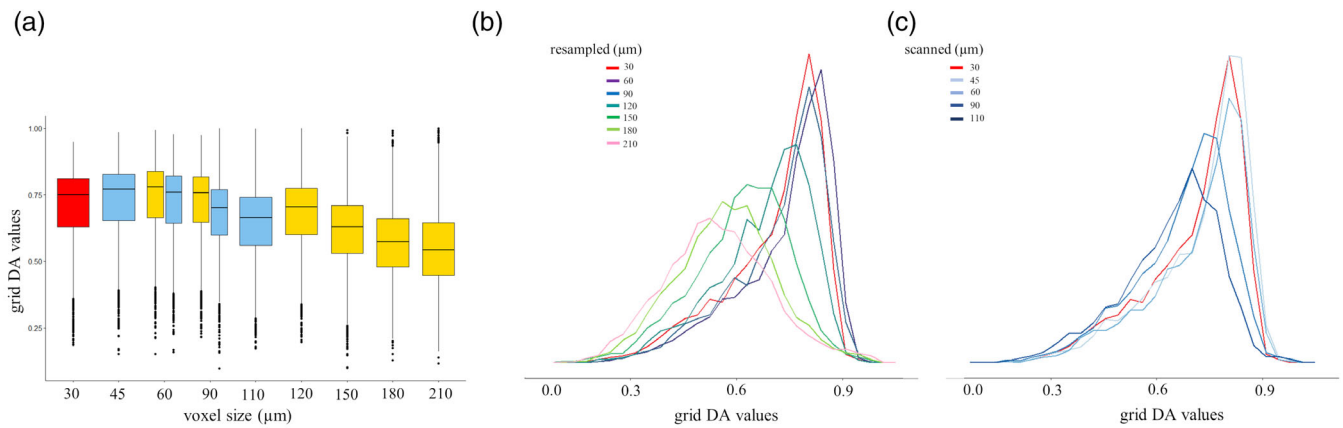
FIGURE 5 (a) Boxplots of the grid DA values for each voxel size for the baseline scan (red), the downsampled data (yellow) and for the specimen scanned at the different resolution (blue); (b) histogram of the grid DA values for each voxel size for the baseline scan (red line) and the downsampled data; (c) histogram of the grid DA values for each voxel size for the baseline scan (red line) and for the specimen scanned at different resolution. DA, degree of anisotropy.

morphology of the distal tibia of a *G. gorilla* individual. Rescanning was found to have a stronger effect on DA and Tb.Th, while BV/TV, Tb.Sp, and Tb.N remained relatively constant across all tested voxel sizes. Downsampling was found to have less of an effect on trabecular parameters compared to rescanning. However, a strong impact on trabecular parameters when downsampling was found in DA and Tb.Th, while BV/TV, Tb.Sp, and Tb.N were less sensitive to increasing voxel sizes.

Quantification of the total BV/TV after segmentation demonstrated differences in the number of bone voxels segmented in each protocol. This BV/TV changed more for rescanned voxel sizes compared to downsampled voxel sizes. However, the differences were below 5% compared to the baseline scan across all scans. When the baseline scan was downsampled to larger voxel sizes, the total segmented BV/TV decreased gradually. However, the opposite pattern was found in rescanned images where the total segmented BV/TV gradually increased with larger voxel sizes. Changes in total segmented BV/TV within the rescanned images often represented fundamental differences that could also be observed on visual inspection of the voxel data. With the lowest scanned resolution, a more substantial difference in volume was found, and the trabecular structure captured is less comparable to that at higher scan resolutions. However, for the results of the downsampled images, where the data captured was based on the voxel set acquired at a higher resolution, there was less divergence in BV/TV from the baseline scan.

Our results for Tb.Th and Tb.Sp imply that while the trabecular spacing remains relatively stable, Tb.Th increases at larger voxel sizes. Because Tb.Sp is higher than Tb.Th, it is less sensitive to scanning/downsampling at tested resolutions. This might suggest that the thickness of the trabeculae is overestimated, that is, trabeculae are segmented as thicker, in very low-resolution scans. Another explanation could be that small trabeculae are lost during the downsampling/rescanning to larger voxels and thus the distribution of the thickness changes more rapidly than it is the case for Tb.Sp. Partial volume averaging occurs when the boundaries of small structures within an image

intersect multiple pixels or voxels. This can lead to a blurring effect, where the intensity values of different tissues or structures are averaged within the pixels or voxels. This can compromise the spatial resolution of the image and make it difficult to accurately delineate the small structures or detect fine details (Chakeres, 1984; Plewes & Dean, 1981). Downsampling/rescanning to larger voxel sizes can exacerbate the effects of partial volume averaging, especially if the original image already contains small structures that are near the limit of resolution. Thus, when an image is downsampled/rescanned, the smaller structures may be spread across even fewer pixels or voxels, increasing the degree of averaging, and further blurring the image, that is, downsampling/rescanning can amplify the problem of partial volume averaging by reducing the number of pixels or voxels available to represent small structures within an image (Chakeres, 1984; Conradi et al., 2010; Plewes & Dean, 1981). Thus, it is possible that in the end only the largest trabeculae persist, giving the impression that the average Tb.Th is as large as the maximum of the initial Tb.Th. Moreover, this partial volume averaging could also explain how BV/TV remains constant despite trabeculae getting thicker (on average). It must be emphasized that the trabecular parameters are measured on the segmented images and thus, the changes in the segmented images are another source of potential error in the measurement of trabecular parameters. As mentioned above, MIA is a voxel-size dependent segmentation method (Dunmore et al., 2018). Although we used the same protocol for each bone segmentation, ultimately any segmentation algorithm is limited by the size of the voxels it is classifying.

Our result suggests that the BV/TV, Tb.Sp, and Tb.N can be measured with reasonable precision up to 210 μm, as can DA and Tb.Th up to 90 μm, when downsampling. In contrast, the mean of BV/TV, DA, Tb.Sp, and Tb.N increases from 90 μm when rescanning. We found Tb.Th to be the most sensitive to voxel size changes, where the mean increased for scans above 45 μm. This is visible especially when looking at the colourmaps of the distribution patterns of all studied parameters. The discrepancies might be
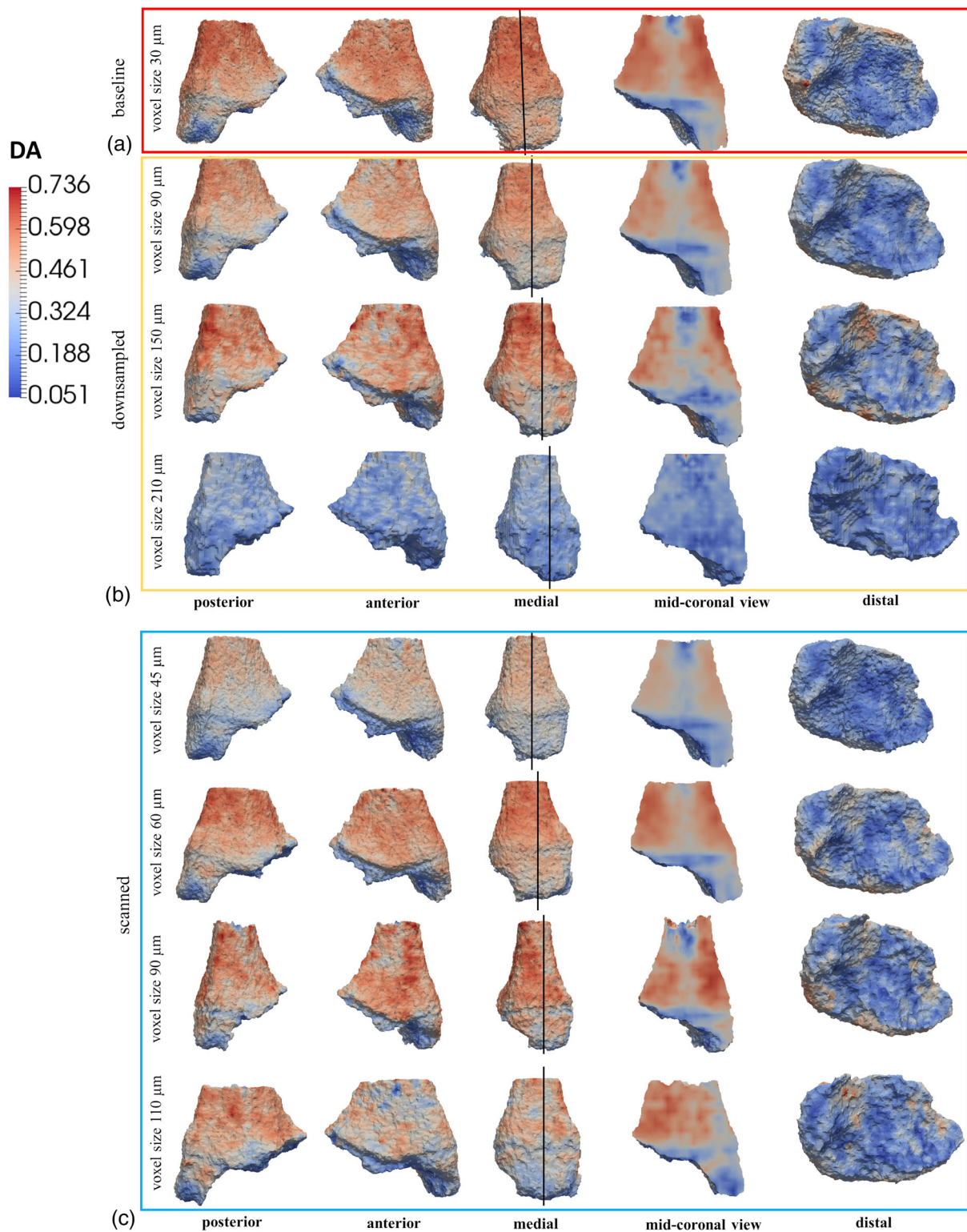
FIGURE 6 Distal tibia model of DA distribution of tested *Gorilla* individual for baseline scan (a), downsampled voxel sizes of 90, 150, and 210 μm (b), and scan voxel sizes of 45–110 μm (c). Vertical lines through the medial view show where the slices are positions for the cross-section mid-coronal view. Dark red represents the highest and dark blue the lowest DA values. All colourmaps were scaled to baseline scan data range. DA, degree of anisotropy.

due to the inconsistencies in the definition of the *InnerMask* as medtool uses morphological filters this is influenced by resolution due to kernel size. However, the morphological filter kernel sizes (in voxels) of the fill algorithm were adjusted for each resolution, so definition of the *OuterMask* and *InnerMask* was kept as consistent as possible.
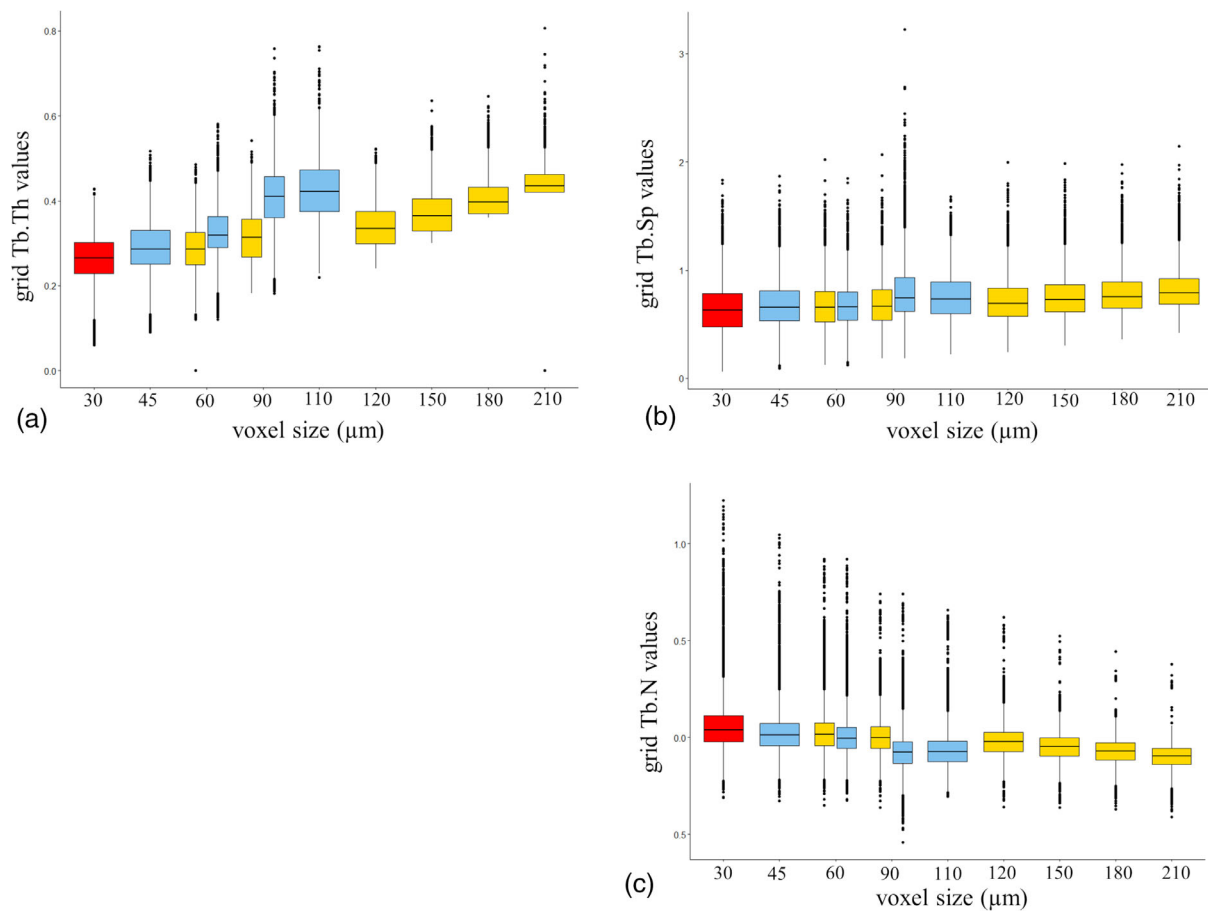
FIGURE 7 Boxplots of the grid Tb.Th (a), Tb.Sp (b), and Tb.N (c) values for each voxel size for the baseline scan (red), the downsampled data (yellow) and for the specimen scanned at the different resolution (blue). Tb.Sp, spacing;Tb.Th, trabecular thickness.

Previous studies of the impact of CT and micro-CT resolution on quantification of trabecular structure observed dependence of trabecular bone parameters on voxel size, consistent with our results. Isaksson et al. (2011) found BV/TV to be less dependent on the voxel sizes compared to DA, Tb.Sp, and Tb.N which were more sensitive to changes in voxel sizes. Similarly, Kim et al. (2004) found mean Tb.Th and Tb.Sp to increase and Tb.N to decrease with larger voxel sizes which is again consistent with our results. However, they also found mean BV/TV to increase significantly with larger voxel sizes (Kim et al., 2004), which is not consistent with our results. Nevertheless, as supported by our study, Christiansen (2016) found mean BV/TV to be rather consistent within the voxel sizes and Tb.Th to be strongly affected by changes in voxel size. Overall, other studies that tested all or some of other trabecular parameters such as Tb.Th, Tb.Sp, and Tb.N have reported higher dependency on voxel size in all these parameters especially compared to BV/TV, and also compared to DA if included in the study (Isaksson et al., 2011; Kim et al., 2004; Kothari et al., 1998; Majumdar et al., 1996; Maquer et al., 2015; Müller et al., 1996; Peyrin et al., 1998; Sode et al., 2008; Stauber et al., 2006; Tabor, 2004).

This study is the first to show the effect of micro-CT voxel size using a whole-bone mapping approach to analyze trabecular bone morphology. Although this study only included a single specimen, and was not extended to other anatomical sites, we recommend using high-resolution if possible. To speed up trabecular analysis, downsampled images rather than low-resolution scans could be used for certain trabecular parameters. This is especially important if DA and Tb.Th are quantified. Our results suggest that trabecular structure may be more precisely measured by quantifying most trabecular parameters up to voxel size of 90 μm (excluding Tb.Th). Moreover, BV/TV, Tb.Sp, and Tb.N are more robust and can be quantified at even larger voxel sizes with a greater degree of certainty than the other parameters, which are more sensitive to voxel size changes.

Though it was beyond the scope of this study, there are additional factors, such as segmentation method and/or the use of multiple micro-CT scanners for sample acquisition that have the potential to impact quantification of trabecular architecture and may warrant future investigation. It is also possible that the effect of voxel size on trabecular bone is different for regions with higher or lower trabecular BV/TV fraction. Thus, including trabecular bone from taxa that differ in mean BV/TV, as well as BV/TV range, is an important future direction. For example, large primates, such as *Gorilla*, tend to have robust trabecular bone network to support their larger body mass. In contrast, small primates generally exhibit relatively less trabecular bone

12 of 14 | **WILEY** AMERICAN JOURNAL OF BIOLOGICAL ANTHROPOLOGY
The Official Journal of the American Association of Biological Anthropologists

LUKOVA ET AL.

structures compared to larger primates as their smaller body size results in lower mechanical loads on their bones, reducing the need for extensive trabecular bone networks (Ryan & Shaw, 2013; Saparin et al., 2011). Based on our results, it might be expected that relatively less trabecular bone structure would be more sensitive to the resolution changes. This could potentially lead to less sensitivity to the resolution changes in BV/TV and potentially other parameters as micro-CT scanning is generally more effective at detecting more gracile structures compared to less gracile structures (e.g., Pyka et al., 2014; Vásárhelyi et al., 2020). Overall, this diversity in sample selection would help address potential sensitivity to resolution changes, particularly in smaller/less more gracile structures, which may lead to a reduction in trabecular network visibility and subsequently affect measured trabecular parameters.

AUTHOR CONTRIBUTIONS

Andrea Lukova: Formal analysis (lead); methodology (lead). **Christopher J. Dunmore:** Formal analysis (equal); methodology (equal). **Zewdi J. Tsegai:** Formal analysis (equal); methodology (equal). **Sebastian Bachmann:** Formal analysis (equal); methodology (equal). **Alexander Synek:** Formal analysis (supporting); methodology (supporting). **Matthew M. Skinner:** Formal analysis (supporting); methodology (supporting).

ACKNOWLEDGMENTS

DATA AVAILABILITY STATEMENT

Copies of all scans are curated by the relevant curatorial institution that is responsible for the original specimen and access can be requested through their institution. The authors confirm that the data supporting the findings of this study are available from the corresponding author upon reasonable request.

ORCID

Andrea Lukova https://orcid.org/0009-0001-9843-336X
Christopher J. Dunmore https://orcid.org/0000-0002-8634-9777
Zewdi J. Tsegai https://orcid.org/0000-0001-9041-4829

REFERENCES

Ahrens, J., Heitmann, K., Habib, S., Ankeny, L., McCormick, P., Inman, J., ... Ma, K. L. (2006). Quantitative and comparative visualization applied to cosmological simulations. *Journal of Physics: Conference Series, 46*, 52–533.

Alberich-Bayarri, A., Marti-Bonmati, L., Sanz-Requena, R., Belloch, E., & Moratal, D. (2008). In vivo trabecular bone morphologic and mechanical relationship using high-resolution 3-T MRI. *American Journal of Roentgenology, 191*, 721–726.

Bachmann, S., Dunmore, C. J., Skinner, M. M., Pahr, D. H., & Synek, A. (2022). A computational framework for canonical holistic morphometric analysis of trabecular bone. *Scientific Reports, 12*, 5187.

Barak, M. M., Lieberman, D. E., & Hublin, J. J. (2011). A Wolff in sheep's clothing: Trabecular bone adaptation in response to changes in joint loading orientation. *Bone, 49*, 1141–1151.

Cazenave, M., Braga, J., Oettlé, A., Pickering, T. R., Heaton, J. L., Nakatsukasa, M., ... Macchiarelli, R. (2019). Cortical bone distribution in the femoral neck of Paranthropus robustus. *Journal of Human Evolution, 135*, 102666.

Chakeres, D. W. (1984). Clinical significance of partial volume averaging of the temporal bone. *American Journal of Neuroradiology, 5*, 297–302.

Christiansen, B. A. (2016). Effect of micro-computed tomography voxel size and segmentation method on trabecular bone microstructure measures in mice. *Bone Reports, 5*, 136–140.

Conradi, S. H., Lutey, B. A., Atkinson, J. J., Wang, W., Senior, R. M., & Gierada, D. S. (2010). Measuring small airways in transverse CT images: Correction for partial volume averaging and airway tilt. *Academic Radiology, 17*, 1525–1534.

DeSilva, J. M., & Devlin, M. J. (2012). A comparative study of the trabecular bony architecture of the talus in humans, non-human primates, and Australopithecus. *Journal of Human Evolution, 63*, 536–551.

Dunmore, C. J., Bardo, A., Skinner, M. M., & Kivell, T. L. (2020). Trabecular variation in the first metacarpal and manipulation in hominids. *American Journal of Physical Anthropology, 171*, 219–241.

Dunmore, C. J., Kivell, T. L., Bardo, A., & Skinner, M. M. (2019). Metacarpal trabecular bone varies with distinct hand-positions used in hominid locomotion. *Journal of Anatomy, 235*, 45–66.

Dunmore, C. J., Skinner, M. M., Bardo, A., Berger, L. R., Hublin, J. J., Pahr, D. H., ... Kivell, T. L. (2020). The position of Australopithecus sediba within fossil hominin hand use diversity. *Nature Ecology & Evolution, 4*, 911–918.

Dunmore, C. J., Wollny, G., & Skinner, M. M. (2018). MIA-clustering: A novel method for segmentation of paleontological material. *PeerJ, 6*, 4374.

Georgiou, L., Dunmore, C. J., Bardo, A., Buck, L. T., Hublin, J. J., Pahr, D. H., ... Skinner, M. M. (2020). Evidence for habitual climbing in a Pleistocene hominin in South Africa. *Proceedings of the National Academy of Sciences, 117*, 8416–8423.

Georgiou, L., Kivell, T. L., Pahr, D. H., & Skinner, M. M. (2018). Trabecular bone patterning in the hominoid distal femur. *PeerJ, 6*, 5156.

Glatt, V., Canalis, E., Stadmeyer, L., & Bouxsein, M. L. (2007). Age-related changes in trabecular architecture differ in female and male C57BL/6J mice. *Journal of Bone and Mineral Research, 22*, 1197–1207.

Goldstein, S. A., Goulet, R., & McCubbrey, D. (1993). Measurement and significance of three-dimensional architecture to the mechanical integrity of trabecular bone. *Calcified Tissue International, 53*, 127–133.

Griffin, C. T. (2018). Pathological bone tissue in a late Triassic neotheropod fibula, with implications for the interpretation of medullary bone. *New Jersey State Museum Investigations, 6*, 2–10.

Gross, T., Kivell, T. L., Skinner, M. M., Nguyen, N. H., & Pahr, D. H. (2014). A CT-image-based method for the holistic analysis of cortical and trabecular bone. *Submitted to pal Elec, 17*, 33A.

Halloran, B. P., Ferguson, V. L., Simske, S. J., Burghardt, A., Venton, L. L., & Majumdar, S. (2002). Changes in bone structure and mass with advancing age in the male C57BL/6J mouse. *Journal of Bone and Mineral Research, 17*, 1044–1050.

He, J., Chen, S., Zhang, H., Tao, X., Lin, W., Zhang, S., ... Ma, J. (2021). Downsampled imaging geometric modeling for accurate CT reconstruction via deep learning. *IEEE Transactions on Medical Imaging, 40*, 2976–2985.

Isaksson, H., Töyräs, J., Hakulinen, M., Aula, A. S., Tamminen, I., Julkunen, P., ... Jurvelin, J. S. (2011). Structural parameters of normal and osteoporotic human trabecular bone are affected differently by microCT image resolution. *Osteoporosis International, 22*, 167–177.

Keaveny, T. M., Morgan, E. F., Niebur, G. L., & Yeh, O. C. (2001). Biomechanics of trabecular bone. *Annual Review of Biomedical Engineering, 3*, 307–333.

Kim, D. G., Christopherson, G. T., Dong, X. N., Fyhrie, D. P., & Yeni, Y. N. (2004). The effect of microcomputed tomography scanning and reconstruction voxel size on the accuracy of stereological measurements in human cancellous bone. *Bone, 35*, 1375–1382.

Kivell, T. L. (2016). A review of trabecular bone functional adaptation: What have we learned from trabecular analyses in extant hominoids and what can we apply to fossils? *Journal of Anatomy, 228*, 569–594.

Kivell, T. L., Skinner, M. M., Lazenby, R., & Hublin, J. J. (2011). Methodological considerations for analyzing trabecular architecture: An example from the primate hand. *Journal of Anatomy, 218*, 209–225.

Kothari, M., Keaveny, T. M., Lin, J. C., Newitt, D. C., Genant, H. K., & Majumdar, S. (1998). Impact of spatial resolution on the prediction of trabecular architecture parameters. *Bone, 22*, 437–443.

Lazenby, R. A., Skinner, M. M., Kivell, T. L., & Hublin, J. J. (2011). Scaling VOI size in 3D μCT studies of trabecular bone: A test of the oversampling hypothesis. *American Journal of Physical Anthropology, 144*, 196–203.

Loewen, T. N., Carriere, B., Reist, J. D., Halden, N. M., & Anderson, W. G. (2016). Linking physiology and biomineralization processes to ecological inferences on the life history of fishes. *Comparative Biochemistry and Physiology Part A: Molecular & Integrative Physiology, 202*, 123–140.

Lukova, A., Dunmore, C. J., Bachmann, S., Synek, A., Pahr, D. H., Kivell, T. L., & Skinner, M. M. (2024). Trabecular architecture of the distal femur in extant hominids. *Journal of Anatomy, 245*, 156–180.

Majumdar, S., Newitt, D., Mathur, A., Osman, D., Gies, A., Chiu, E., … Genant, H. (1996). Magnetic resonance imaging of trabecular bone structure in the distal radius: Relationship with X-ray tomographic microscopy and biomechanics. *Osteoporosis International, 6*, 376–385.

Maquer, G., Musy, S. N., Wandel, J., Gross, T., & Zysset, P. K. (2015). Bone volume fraction and fabric anisotropy are better determinants of trabecular bone stiffness than other morphological variables. *Journal of Bone and Mineral Research, 30*, 1000–1008.

Müller, R., Koller, B., Hildebrand, T., Laib, A., Gianolini, S., & Rüegsegger, P. (1996). Resolution dependency of microstructural properties of cancellous bone based on three-dimensional μ-tomography. *Technology and Health Care, 4*, 113–119.

Müller, R., & Rüegsegger, P. (1996). Analysis of mechanical properties of cancellous bone under conditions of simulated bone atrophy. *Journal of Biomechanics, 29*, 1053–1060.

Odgaard, A., Kabel, J., van Rietbergen, B., Dalstra, M., & Huiskes, R. (1997). Fabric and elastic principal directions of cancellous bone are closely related. *Journal of Biomechanics, 30*, 487–495.

Pahr, D. H., & Zysset, P. K. (2009). From high-resolution CT data to finite element models: Development of an integrated modular framework. *Computer Methods in Biomechanics and Biomedical Engineering, 12*, 45–57.

Paternoster, L., Lorentzon, M., Lehtimäki, T., Eriksson, J., Kähönen, M., Raitakari, O., … Ohlsson, C. (2013). Genetic determinants of trabecular and cortical volumetric bone mineral densities and bone microstructure. *PLoS Genetics, 9*, 1003247.

Peyrin, F., Salome, M., Cloetens, P., Laval-Jeantet, A. M., Ritman, E., & Rüegsegger, P. (1998). Micro-CT examinations of trabecular bone samples at different resolutions: 14, 7 and 2 micron level. *Technology and Health Care, 6*, 391–401.

Plewes, D. B., & Dean, P. B. (1981). The influence of partial volume averaging on sphere detectability in computed tomography. *Physics in Medicine & Biology, 26*, 913–919.

Pontzer, H., Lieberman, D. E., Momin, E., Devlin, M. J., Polk, J. D., Hallgrimsson, B., & Cooper, D. M. L. (2006). Trabecular bone in the bird knee responds with high sensitivity to changes in load orientation. *Journal of Experimental Biology, 209*, 57–65.

Pyka, G., Kerckhofs, G., Schrooten, J., & Wevers, M. (2014). The effect of spatial micro-CT image resolution and surface complexity on the morphological 3D analysis of open porous structures. *Materials Characterization, 87*, 104–115.

Ruff, C., Holt, B., & Trinkaus, E. (2006). Who's afraid of the big bad Wolff?: "Wolff's law" and bone functional adaptation. *American Journal of Physical Anthropology, 129*, 484–498.

Ryan, T. M., & Shaw, C. N. (2012). Unique suites of trabecular bone features characterize locomotor behavior in human and non-human anthropoid primates. *PLoS One, 7*, e41037.

Ryan, T. M., & Shaw, C. N. (2013). Trabecular bone microstructure scales allometrically in the primate humerus and femur. *Proceedings of the Royal Society B: Biological Sciences, 280*, 20130172.

Saers, J. P., Ryan, T. M., & Stock, J. T. (2020). Baby steps towards linking calcaneal trabecular bone ontogeny and the development of bipedal human gait. *Journal of Anatomy, 236*, 474–492.

Saparin, P., Scherf, H., Hublin, J. J., Fratzl, P., & Weinkamer, R. (2011). Structural adaptation of trabecular bone revealed by position resolved analysis of proximal femora of different primates. *The Anatomical Record: Advances in Integrative Anatomy and Evolutionary Biology, 294*, 55–67.

Schulte, F. A., Ruffoni, D., Lambers, F. M., Christen, D., Webster, D. J., Kuhn, G., & Müller, R. (2013). Local mechanical stimuli regulate bone formation and resorption in mice at the tissue level. *PLoS One, 8*, 62172.

Seeman, E. (2003). Bone quality. *Osteoporosis International, 14*, 3–7.

Sinclair, K. D., Farnsworth, R. W., Pham, T. X., Knight, A. N., Bloebaum, R. D., & Skedros, J. G. (2013). The artiodactyl calcaneus as a potential control bone cautions against simple interpretations of trabecular bone adaptation in the anthropoid femoral neck. *Journal of Human Evolution, 64*, 366–379.

Sode, M., Burghardt, A. J., Nissenson, R. A., & Majumdar, S. (2008). Resolution dependence of the non-metric trabecular structure indices. *Bone, 42*, 728–736.

Stauber, M., Rapillard, L., van Lenthe, G. H., Zysset, P., & Müller, R. (2006). Importance of individual rods and plates in the assessment of bone quality and their contribution to bone stiffness. *Journal of Bone and Mineral Research, 21*, 586–595.

Su, A., Wallace, I. J., & Nakatsukasa, M. (2013). Trabecular bone anisotropy and orientation in an early Pleistocene hominin talus from East Turkana, Kenya. *Journal of Human Evolution, 64*, 667–677.

Sylvester, A. D., & Terhune, C. E. (2017). Trabecular mapping: Leveraging geometric morphometrics for analyses of trabecular structure. *American Journal of Physical Anthropology, 163*, 553–569.

Tabor, Z. (2004). Analysis of the influence of image resolution on the discriminating power of trabecular bone architectural parameters. *Bone, 34*, 170–179.

Tsegai, Z. J., Kivell, T. L., Gross, T., Nguyen, N. H., Pahr, D. H., Smaers, J. B., & Skinner, M. M. (2013). Trabecular bone structure correlates with hand posture and use in hominoids. *PLoS One, 8*, 78781.

Turner, C. H., Hsieh, Y. F., Müller, R., Bouxsein, M. L., Baylink, D. J., Rosen, C. J., … Beamer, W. G. (2000). Genetic regulation of cortical and trabecular bone strength and microstructure in inbred strains of mice. *Journal of Bone and Mineral Research, 15*, 1126–1131.

Tward, D. J., & Siewerdsen, J. H. (2009). Noise aliasing and the 3D NEQ of flat-panel cone-beam CT: Effect of 2D/3D apertures and sampling. *Medical Physics, 36*, 3830–3843.

Ulrich, D., Van Rietbergen, B., Laib, A., & Ruegsegger, P. (1999). The ability of three-dimensional structural indices to reflect mechanical aspects of trabecular bone. *Bone, 25*, 55–60.

Van Rietbergen, B., Odgaard, A., Kabel, J., & Huiskes, R. (1998). Relationships between bone morphology and bone elastic properties can be

accurately quantified using high-resolution computer reconstructions. *Journal of Orthopaedic Research*, 16, 23–28.

Vásárhelyi, L., Kónya, Z., Kukovecz, Á., & Vajtai, R. (2020). Microcomputed tomography–based characterization of advanced materials: A review. *Materials Today Advances*, 8, 100084.

Whitehouse, W. J. (1974). The quantitative morphology of anisotropic trabecular bone. *Journal of Microscopy*, 101, 153–168.

Wickham, H. (2016). *ggplot2: Elegant graphics for data analysis*. Springer-Verlag. https://ggplot2.tidyverse.org

Yen, S. Y., Yan, C. H., Rubin, G. D., & Napel, S. (1999). Longitudinal sampling and aliasing in spiral CT. *IEEE Transactions on Medical Imaging*, 18, 43–58.

Zbijewski, W., & Beekman, F. J. (2003). Characterization and suppression of edge and aliasing artefacts in iterative x-ray CT reconstruction. *Physics in Medicine & Biology*, 49, 145.

SUPPORTING INFORMATION

Additional supporting information can be found online in the Supporting Information section at the end of this article.

How to cite this article: Lukova, A., Dunmore, C. J., Tsegai, Z. J., Bachmann, S., Synek, A., & Skinner, M. M. (2024). Technical note: Does scan resolution or downsampling impact the analysis of trabecular bone architecture? *American Journal of Biological Anthropology*, e25023. https://doi.org/10.1002/ajpa.25023